Continuum analysis of an avalanche model for solar flares

Han-Li Liu,[1] Paul Charbonneau,[1] Annick Pouquet,[2] Thomas Bogdan,[1] and Scott McIntosh[3]

[1]*High Altitude Observatory, National Center for Atmospheric Research, P.O. Box 3000, Boulder, Colorado 80307*

[2]*Advanced Study Program, National Center for Atmospheric Research, P.O. Box 3000, Boulder, Colorado 80307*

[3]*ESA Research and Scientific Support Department, NASA Goddard Space Flight Center, Mailcode 682.3, Greenbelt, Maryland 20771*

We investigate the continuum limit of a class of self-organized critical lattice models for solar flares. Such models differ from the classical numerical sandpile model in their formulation of stability criteria in terms of the curvature of the nodal field, and are known to belong to a different universality class. A fourth-order nonlinear hyperdiffusion equation is reverse engineered from the discrete model's redistribution rule. A dynamical renormalization-group analysis of the equation yields scaling exponents that compare favorably with those measured in the discrete lattice model within the relevant spectral range dictated by the sizes of the domain and the lattice grid. We argue that the fourth-order nonlinear diffusion equation that models the behavior of the discrete model in the continuum limit is, in fact, compatible with magnetohydrodynamics (MHD) of the flaring phenomenon in the regime of strong magnetic field and the effective magnetic diffusivity characteristic of strong MHD turbulence.

I. INTRODUCTION: SOLAR FLARES AS AVALANCHES

With the so-called solar neutrino problem now turned over to particle physicists, coronal heating remains arguably the grand unsolved problem of the contemporary solar physics. There is general agreement that the energy source maintaining the temperature of the coronal plasma in excess of 10^6 K against radiative and conductive losses is, ultimately, the mechanical energy associated with convective fluid motions. However, the manner in which this mechanical energy is converted to thermal energy within the corona has yet to be elucidated.

One very attractive mechanism was proposed nearly two decades ago by Parker (e.g., Refs. [1–3]). In his picture, the mechanical energy is first stored as magnetic energy within photospherically anchored coronal magnetic structures (the "coronal loops" ubiquitous in the corona), and subsequently transferred to the plasma by reconnection mediated *in situ* dissipation of the magnetic field. The general idea is illustrated in Fig. 1. The left panel shows a "straightened" coronal loop, where the upper and lower bounding surfaces correspond to the two regions of the solar photosphere where the loop is anchored. At photospheric levels, the magnetic field is too weak to resist the stochastic horizontal fluid motions associated with convection and granulation, so that the footpoints of the initially uniform magnetic field lines ($t=t_0$) are randomly shuffled. After many flow turnover times ($t=t_1$), the field lines end up complexly wrapped around one another. As the coronal field continuously attempts to relax to a force-free state in response to this boundary forcing, the current sheets inexorably build up in regions where field lines kink around one another. In view of the high electrical conductivity of the coronal plasma, these sheets become very thin and pervaded by very intense electrical currents, which eventually become subject to an assortment of plasma instabilities. Magnetic reconnection then sets in, leading to the local release of magnetic energy and reconfiguration of the magnetic field in and around the dissipating

sheets. Order-of-magnitude estimates of the energy released by such dissipative events are around 10^{24} erg, about nine orders of magnitude smaller than a typical large solar flare. Thus the name "nanoflare" was coined by Parker [2], who moreover conjectured that the collective energy released by the ensemble of nanoflares continuously occurring throughout the magnetized corona is a sufficient energy input for coronal heating.

Although it was not originally emphasized in Parker's coronal heating model, his picture of an externally stressed, complexly tangled coronal magnetic field incorporates all required ingredient for a self-organized critical (SOC) avalanche model: (1) an open physical system driven by slow, external forcing; (2) subject to a self-stabilizing threshold instability; and (3) leading to localized redistribution of an associated dynamical variable [4,5]. The dissipation of the
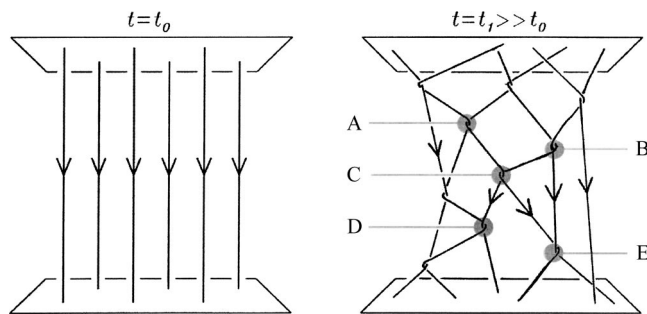

FIG. 1. Buildup of tangential discontinuities (sites labeled "*A*," "*B*," etc., on right panel) in response to boundary forcing of an initially uniform magnetic field (left panel), as envisioned within Parker's conjecture of coronal heating by nanoflares. The structure on the left panel is an idealized representation of a straightened coronal magnetic loop anchored in the solar photosphere, the latter corresponding to the upper and lower bounding "plates" (see text). Reconnection-mediated dissipative events at site *C* affect the magnetic field at neighboring sites (A,B,D,E), any of which in turn possibly undergoing dissipative reconfiguration, leading to an avalanche of dissipative events cascading through the system.

small current sheets (e.g., site "*C*" on Fig. 1), which Parker associates with nanoflares, can alter the physical conditions at neighboring current sheets (sites *A*, *B*, *D*, and *E*), possibly triggering further dissipative events at these locations, and so on across the whole stressed coronal structure. Parker's physical picture can thus be readily reinterpreted as a general avalanche model for solar flares of all sizes.

Inspired by Parker's nanoflare picture, as well as the classical SOC numerical sandpile models [6,7], Lu and coworkers have developed a sandpilelike SOC avalanche model applicable to solar flares ([8,9], hereafter Lu-Hamilton 91 (LH91) and Lu-Hamilton-McTiernan-Bromund (LHMB), respectively; see also Refs. [4,10]). In their models the dynamical variable is some measure of the magnetic field defined on a lattice, and the model differs from the "canonical" sandpile models in defining its stability criterion in terms of the field *curvature* (more on this in Sec. II below; for a recent review, see also Ref. [11]). Although it belongs to a different universality class [12], this variation of the sandpile model behaves much like the better-known height- or gradient-triggered versions of the sandpile model, in that it is naturally driven to a self-organized critical state characterized by avalanches with a power-law size spectrum.

The basic LH91/LHMB avalanche model has met with remarkable success in reproducing the observed statistical properties of solar flares. The power-law form of the frequency distribution of observed flare parameters arises naturally from the self-similarity characterizing the avalanching process in the SOC state. Moreover, most logarithmic slopes predicted by the model are in reasonable agreement with their observationally inferred counterparts [9,11,13,14]. For the present, the most serious discrepancy is the power-law index of the frequency distributions for the flaring area; the model power-law distribution is significantly flatter than observations [15]. While these most recent results pose a serious challenge to the nanoflare mechanism of coronal heating, the avalanche model inspired by Parker's physical picture of photospherically stressed, complexly tangled coronal magnetic field remains a very promising explanatory model for flares, in general.

These successes motivate further exploration of the model's behavior, and, in particular, on those aspects of the model that influence the power-law slopes of the size distributions of avalanche parameters. Various authors have pointed out that the redistribution rules of the flare avalanche model amount to a transport of the dynamical variable akin to a diffusionlike process [10,16–18]. Since assorted high-order diffusion-type equations are well known to exhibit self-similar solutions characterized by self-similar avalanching behavior (see, e.g., [19–22]), further exploration of the analogy between the (discrete) avalanche model and (continuum) high-order diffusive systems is warranted. This is the primary purpose of this paper. In Sec. II, we begin by reverse engineering a fourth-order continuum hyperdiffusion equation, whose discretization by centered finite differences leads to update rules identical to the redistribution rules of the LH91 avalanche model. We then perform a von Neumann stability analysis of this hyperdiffusion equation. This allows us to clarify some subtle behavioral differences between the

LH91 and LHMB versions of the solar flare avalanche model. In Sec. III, we carry out a dynamical renormalization-group (DRG) analysis of our hyperdiffusion equation and determine the invariants of the DRG transformation. Then in Sec. IV, these invariants are used to derive the power-law slopes of several quantities and these slopes are compared to the results from the avalanche models. The good agreement found therein suggests that our derived continuum hyperdiffusion has indeed "captured" the essence of the spatially discrete avalanche model. We conclude in Sec. V by speculating on the possible connections between the hyperdiffusive threshold-triggered transport and magnetic reconnection in the high electrical conductivity, magnetically dominated coronal plasma.

II. CONTINUUM LIMIT OF THE CURVATURE-TRIGGERED AVALANCHE MODELS

As with most sandpile models, the LH91 (and LHMB) avalanche model employs a stability criterion and a redistribution rule to evolve a field variable defined on a discrete lattice, subject to the action of a random driver operating only when the system is not avalanching (the so-called slow driving limit). However, and in contrast to the classical sandpile model, the stability criterion is defined in terms of the local *curvature* of the field, rather than its height or gradient. For a scalar field *A* defined on a one-dimensional lattice, the stability measure is thus expressed in terms of

$$\Delta A_i^n \equiv A_i^n - \frac{1}{2} \sum_{j=i\pm 1} A_j^n. \tag{1}$$

If $|\Delta A|$ at node i is larger than a prespecified critical value A_c, then A will redistribute according to

$$A_i^{n+1} = A_i^n - \frac{2}{3} \Delta A_i^n, \tag{2a}$$

$$A_{i\pm 1}^{n+1} = A_{i\pm 1}^n + \frac{1}{3} \Delta A_i^n, \tag{2b}$$

in the LH91 modeling framework. The total *A* is conserved in the process of the redistribution, and the local curvature ΔA_i becomes 0 after the redistribution.

According to this redistribution rule, and under the assumption of synchronous nodal updating, each node is subject to three individual increment/decrement operations in a region where contiguous nodes are avalanching:

$$A_i^{n+1} = A_i^n - \frac{2}{3} \Delta A_i^n + \frac{1}{3} \Delta A_{i+1}^n + \frac{1}{3} \Delta A_{i-1}^n. \tag{3}$$

Let $A^n \equiv [A_i^n]$, so that Eq. (3) can be expressed in the equivalent matrix form

$$A^{n+1} - A^n = -\frac{2}{3} [S][S] A^n, \tag{4}$$
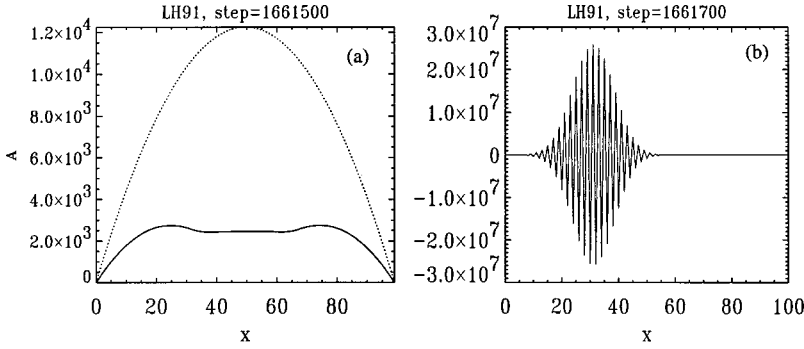
where

FIG. 2. Two snapshots of the scalar nodal field A in a one-dimensional LH91 avalanche model run. The system rapidly becomes unstable shortly after it begins avalanching, and long before reaching the SOC state which here is characterized by a parabolic profile in x as shown by the dotted line in panel (a). Panels (a) and (b) are 200 iterations apart. The model was initialized with $A=0$ at all nodes, and driven with random increments uniformly distributed in the range $[-0.4, 0.6]$, with the stability threshold set at $A_c = 7$.

$$[S]_{i,j} = \delta_{i,j} - \frac{1}{2}\delta_{i,j+1} - \frac{1}{2}\delta_{i,j-1}, \tag{5}$$

and $\delta_{i,j}$ is the Kronecker delta. Designate the spatial dimension as x and the node interval as the unit length $\Delta x = 1$, then $[S]$ is the second-order centered finite difference operator of $-1/2(\partial^2/\partial x^2)$. Equation (4) is then the time-forward differencing integration of the hyperdiffusion equation

$$\frac{\partial A}{\partial t} = -\kappa\frac{\partial^4 A}{\partial x^4}, \tag{6}$$

with $\kappa = 1/6$ and a unit "time step" $\Delta t = 1$. Therefore, repeated application of Eqs. (2) in an avalanching portion of the lattice is equivalent to a finite difference integration of the hyperdiffusion equation (6).

Carrying out a standard von Neumann stability analysis [23], on Eq. (4), yields the following amplification factor (p) for this scheme:

$$p = 1 - 4\kappa\frac{\Delta t}{\Delta x^4}(\cos k\Delta x - 1)^2. \tag{7}$$

For unit temporal and spatial intervals and $\kappa = 1/6$, $\max|p| = 5/3$. Therefore, the finite difference (4) is unconditionally unstable. This has been verified in our numerical experiment using LH91, as shown in Fig. 2. The parabolic curve (dotted) in the plot is an approximation to the A field in the SOC state obtained from LHMB, where the threshold is set to the same value as in this LH91 model ($A_c = 7$). It is seen from Fig. 2 that LH91 becomes unstable shortly after it begins avalanching and the system is still far from the SOC state. This numerical instability can be easily corrected by reducing the diffusion coefficient from $1/6$ to $\alpha/6$ ($\alpha < 1$), which is equivalent to reducing the redistributed quantity [ΔA in Eqs. (2)] by a factor α. In view of Eq. (7) above, α should be less than $3/4$ to ensure stability. Numerical experiments using the LH91 formalism but with reduced redistribution were conducted, yielding now a stable algorithm and a solution building up to a *bona fide* SOC state.

In the LHMB model, the stability criterion is the same as that in LH91, but the redistribution is reduced from $|\Delta A|$ to A_c. This is equivalent to multiplying a factor $A_c/|\Delta A|$, which is less than 1 in avalanching regions, to the redistributed quantity. The numerically stable behavior of the LHMB model is thus consistent with the above analysis. In fact, the introduction of this reduction factor makes the net adjust-

ment at each node interior of a contiguous avalanching region zero according to Eq. (3). Therefore, in LHMB, all adjustments due to avalanching occur near the boundary between avalanching and nonavalanching regions.

In stable regions of the lattice, there is obviously no redistribution of A and thus Eq. (6) holds provided one sets $\kappa = 0$. At the boundary between the avalanching and stable regions, however, the above derivation needs to be modified because the redistribution has a spatial dependence. A more general form of Eq. (3) should thus be

$$A_i^{n+1} = A_i^n - 4\kappa_i^n \Delta A_i^n + 2\kappa_{i+1}^n \Delta A_{i+1}^n + 2\kappa_{i-1}^n \Delta A_{i-1}^n, \tag{8a}$$

$$\kappa_i = \begin{cases} \kappa_a & \text{if } \Delta A^2 > A_c^2, \\ 0 & \text{otherwise} \end{cases}, \tag{8b}$$

where κ_a is equal to $1/6$ for the original LH91 formulation. Equations (8) can be formally viewed as a finite difference equation for

$$\frac{\partial A}{\partial t} = -\frac{\partial^2}{\partial x^2}\kappa(A_{xx}^2)\frac{\partial^2 A}{\partial x^2}, \tag{9}$$

where $\kappa(A_{xx}^2)$ indicates that the diffusion coefficient κ is a function of the value of local curvature A_{xx}^2 (the absolute value $|A_{xx}|$ is not used because it may not be differentiable). However, the subgrid feature of κ in Eq. (8) is not given by the avalanche model and is implicitly scale dependent. To further study the avalanche system in the continuum limit, it is thus necessary to *construct* a κ that approximates the discrete step function (8b) (e.g., a hyperbolic tangent function). As can be seen in later discussions, the detailed form of κ is not important in studying the statistical features of the system.

Equation (9) can also describe more general systems with varying diffusion coefficients (varying redistribution) inside avalanching regions, such as LHMB. For LHMB, $\kappa \propto 1/\sqrt{(\partial^2 A/\partial x^2)^2}$ inside an avalanching region (but not near its boundaries), so the net diffusion there is zero. That the two systems, modified LH91 and LHMB, can be described by the same equation is consistent with the fact that both the systems display SOC behavior with similar statistical features. Both model variations belong to the same universality class, and the detailed form of $\kappa(A_{xx}^2)$ is largely irrelevant.

Assuming that $\kappa(A_{xx}^2)$ is second-order differentiable with respect to A_{xx}^2, Eq. (9) can be rewritten as

$$\frac{\partial A}{\partial t} = -\kappa_1 \frac{\partial^4 A}{\partial x^4} - \kappa_2 \frac{\partial^2 A_{xx}^3}{\partial x^2} - \kappa_3 \frac{\partial^2 A_{xx}^5}{\partial x^2}, \qquad (10)$$

where κ_i are all functions of A_{xx}^2. This equation thus describes the diffusion of the first (linear), third, and fifth power of the curvature on a spatial scale of the order of the grid size (unit 1) for the avalanche model. Our goal, characteristic of the study of critical phenomena, is to derive the large-scale statistical features of the system and the scaling behavior of A and κ_i from Eq. (10) that describes the *local* behavior of the avalanching system. The form of the equation will be the same in the process of scale transformation, while the details (i.e., higher wave number components) of the coefficients are irrelevant. For example, the exact diffusion coefficient can be highly variable among the lattice grids and between time steps in the avalanche model. However, the associated high wave number and high frequency components will be eliminated in the process of coarse graining and thus become irrelevant for the study of the large-scale behavior. For this study, we will focus on the cubic nonlinear term, study its correction to the hyperdiffusion term, and omit the fifth-order nonlinear term. With these considerations and also taking into account the random driving of the system, the following equation can be constructed to represent the curvature-triggered avalanche system in the continuum limit:

$$\frac{\partial A}{\partial t} = -\nu \frac{\partial^4 A}{\partial x^4} - \lambda \frac{\partial^2 A_{xx}^3}{\partial x^2} + F_R, \qquad (11)$$

where ν is the hyperdiffusion coefficient and λ is the nonlinear coupling coefficient; F_R is a random driving that will be defined in spectral space in the following section. It should be noted here that, in the avalanche models (LH91 and LHMB), the mean (dc component) of the random driving is a nonzero constant so that a mean field builds up. It is characteristic of these systems that a statistical equilibrium be reached after a certain number of iterations when the statis-

tical mean of the total ''energy'' of the system becomes a constant and the overall curvature of the system remains close to the critical value A_c. All of the following analyses will be based on SOC lattice solutions having reached this statistical equilibrium.

III. DYNAMICAL RENORMALIZATION-GROUP ANALYSIS OF THE SYSTEM

Equipped with Eq. (11), we hope to understand the self-organized critical behavior of the avalanche models LH91 and LHMB by analyzing the critical dynamics of its continuum limit. As mentioned in Sec. I, the various power-law indices may be related to the invariants of DRG transformation of the system. In this section, we will determine the invariants in the DRG transformation of Eq. (11).

Before the DRG analysis, it is necessary to conduct one more transformation on Eq. (11) to remove the second-order derivative of the cubic nonlinear term, so that the perturbative calculation of the nonlinear terms could be carried out conveniently. To achieve this transformation, we take second-order derivatives with respect to x of both sides of Eq. (11) and replace A_{xx} with a new field variable B. Equation (11) then becomes

$$\frac{\partial B}{\partial t} = -\nu \frac{\partial^4 B}{\partial x^4} - \lambda \frac{\partial^4 B^3}{\partial x^4} + F_{Rxx} \qquad (12)$$

with $B \equiv A_{xx}$. On local scales, there should be extra terms with first-and second-order derivatives of ν and λ on the right-hand side (rhs) of the equation. However, only the small wave number and low frequency components are of interest in the DRG analysis, and it is assumed that the derivatives of ν and λ are relatively small and consequently dropped from the equation. An additional benefit of this transformation is that the current random driving term F_{Rxx} is now free of any dc component.

Following the procedures prescribed by Refs. [24] and [25] [Foster-Nelson-Stephen (FNS) hereafter], the DRG analysis is carried out in spectral space. First, Eq. (12) is Fourier transformed with respect to x and t and can be written as

$$-i\omega \hat{B} = -\nu k^4 \hat{B} - \lambda k^4 \int_{k_{1,2}\omega_{1,2}} \hat{B}(k_1, \omega_1) \hat{B}(k_2, \omega_2) \hat{B}(k - k_1 - k_2, \omega - \omega_1 - \omega_2) - k^2 \hat{f}(k, \omega), \qquad (13)$$

or equivalently as

$$\hat{B}(k, \omega) = -G(k, \omega) k^2 \hat{f}(k, \omega) - G(k, \omega) \lambda k^4$$

$$\times \int_{k_{1,2}\omega_{1,2}} \hat{B}(k_1, \omega_1) \hat{B}(k_2, \omega_2)$$

$$\times \hat{B}(k - k_1 - k_2, \omega - \omega_1 - \omega_2), \qquad (14)$$

where G is the propagator

$$G(k, \omega) = \frac{1}{-i\omega + \nu k^4}, \qquad (15)$$

where $k_{1,2}$ and $\omega_{1,2}$ indicate the domain of integration on wave numbers and frequencies stemming from mode coupling due to the cubic nonlinearity of Eq. (12), and the hat denotes the Fourier transform of the corresponding quantities. The ac component of the random driving is now defined as
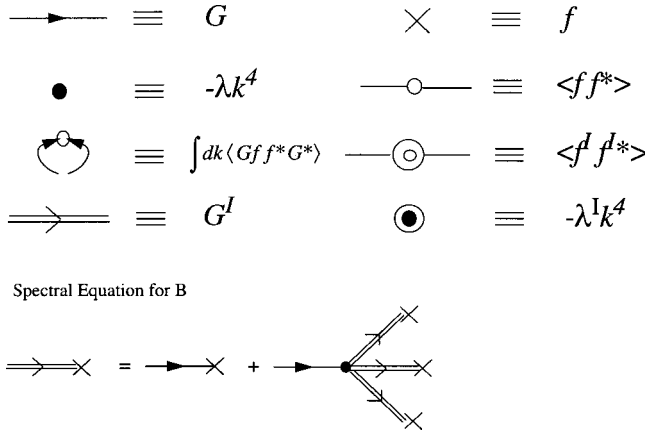
Spectral Equation for B

FIG. 3. Definition of the diagram elements. The diagram expression of Eq. (14) is also given.

$$\langle \hat{f}(k,\omega)\hat{f}(k',\omega')\rangle = 2\pi D k^{-r}\delta(k+k')\delta(\omega+\omega'),$$
(16)

where D measures the strength of the random driving correlation. For the uniform random driving used in the present avalanche models, $r=0$. However, in the models the random driving is applied only during periods when the system is not avalanching, which creates a separation of time scales between avalanching and driving. The random driving defined here is convenient for our analysis, but it imposes a certain limit on the frequency range over which the analysis is applicable, as further discussed below.

The DRG analysis is primarily concerned with the long wavelength mode ($k\to 0$) behavior of the system in the process of coarse graining. In the Fourier transform above, there is a short wavelength (large k) cutoff at a nominal wave number Λ. In the process of coarse graining, the system from Λ to $e^{-l}\Lambda$ ($l>0$), one needs to examine the corrections introduced by the components in the wave number shell $e^{-l}\Lambda<|k|<\Lambda$ on the coarse grained system, specifically, the corrections to the propagator, the nonlinear coupling coefficient λ, and the random driving correlation, in wave number space $|k|<e^{-l}\Lambda$. The corrections to these quantities can be calculated perturbatively using a diagram method similar to those used in FNS and in Ref. [26] (HK92 hereafter). The elements of the diagrams and the diagram equivalence of Eq. (14) are defined in Fig. 3. Equation (14) is, however, cubic nonlinear rather than quadratic nonlinear as in FNS and HK92, and the so-called first Kraichnan-Wyld approximation has been used to determine the perturbation expansion, following Ref. [27]. This is shown in Fig. 4. We note that the vertex equation [Fig. 4(b)] is an approximation rather than being accurate to all orders as in HK92. This is because Eq. (12) is not Galilean invariant, although Eq. (11) before the derivative transformation is. Diagram equations in Figs. 4(a) and 4(b) correspond to

$$\lambda^I=\lambda,$$
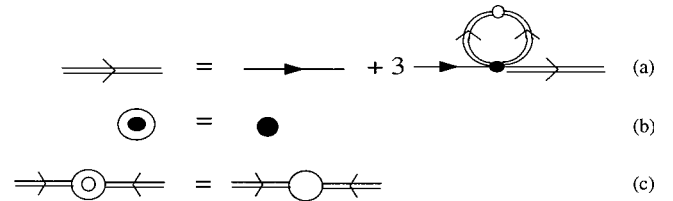(17a)

$$D^I=D.$$
(17b)

FIG. 4. Diagram expression of the first Kraichnan-Wyld approximation; (b) and (c) simply indicate that there is no renormalization of either the force coefficient or the vertex function, the latter by assumption in keeping with the case where Galilean invariance prevails.

The intermediate propagator G^I can be obtained from diagram equation in Fig. 4(a),

$$G^I=\frac{1}{G^{-1}+3\lambda Mk^4}=\frac{1}{-i\omega+(\nu+3\lambda M)k^4},$$
(18)

where M is the mean square displacement

$$M=\frac{1}{(2\pi)^2}\int_{e^{-l}\Lambda}^{\Lambda}dk\int_0^\infty d\omega\frac{k^4\langle\hat{f}(k,\omega)\hat{f}^*(k,\omega)\rangle}{\omega^2+(\nu+3\lambda M)^2k^8}$$

$$=\int_{e^{-l}\Lambda}^{\Lambda}dk\frac{Dk^{-r}}{\nu+3\lambda M},$$
(19)

and the * denotes complex conjugation. Equation (19) can be solved for M, after which the intermediate diffusion coefficient ν^I can be found from Eq. (18),

$$\nu^I=\begin{cases}\nu\left(1+3\rho^2\dfrac{e^{(r-1)l}-1}{r-1}\Lambda^{-r+1}\right) & \text{if } r\neq 1\\[2mm] \nu(1+3\rho^2 l) & \text{if } r=1\end{cases},$$
(20)

where

$$\rho=\frac{\sqrt{\lambda D}}{\nu},$$
(21)

and Eq. (20) is obtained by Taylor expanding one of the exact quadratic solutions (the other one corresponds to a near zero solution) and retaining the second order in ρ. Note that the parameter ρ is akin to a Reynolds number and is the dimensionless control parameter of the problem. Equation (20) also manifests the fluctuation-dissipation theorem for this system, with the diffusivity modified by the random driving through nonlinear coupling.

The wave number k should then be rescaled in such a way that the wave number "sphere" $0<|k|<e^{-l}\Lambda$ is rescaled back to $0<|k_s|<\Lambda$, and in physical space this corresponds to $x=e^l x_s$. With this rescaling, we assume that the time t and the field B scale as

$$t=e^{c_1 l}t_s,$$
(22a)

$$B=e^{c_2 l}B_s,$$
(22b)

or equivalently in spectral space

$$\omega = e^{-c_1 l}\omega_s, \tag{23a}$$

$$\hat{B} = e^{(c_1+c_2+1)l}\hat{B}_s, \tag{23b}$$

and the random forcing $\hat{f}$ scales as

$$\hat{f} = e^{[(r+1+c_1)/2]l}\hat{f}_s. \tag{24}$$

Rescale Eq. (13) using Eqs. (23) and (24) and, by balancing the dimensions, the scaling of ν, λ, and D can be found to be

$$\nu_s = \nu e^{(c_1-4)l}, \tag{25a}$$

$$\lambda_s = \lambda e^{(c_1+2c_2-4)l}, \tag{25b}$$

$$D_s = D e^{(c_1-2c_2+r-5)l}. \tag{25c}$$

The corresponding recursion relations can then be found by combining Eqs. (17), (20), and (25). For $r \neq 1$,

$$\nu_R = \nu e^{(c_1-4)l}\left(1 + 3\rho_R^2 \frac{1-e^{-(r-1)l}}{r-1}\right), \tag{26a}$$

$$\lambda_R = \lambda e^{(c_1+2c_2-4)l}, \tag{26b}$$

$$D_R = D e^{(c_1-2c_2+r-5)l}. \tag{26c}$$

Here $\rho_R^2 = \rho^2 e^{(r-1)l}$ from Eqs. (21) and (25). Because Λ is a reference wave number, it has been set to 1 here for convenience and without loss of generality. The differential recursion relations for λ and D are thus

$$\frac{1}{\lambda_R}\frac{d\lambda_R}{dl} = c_1 + 2c_2 - 4, \tag{27a}$$

$$\frac{1}{D_R}\frac{dD_R}{dl} = c_1 - 2c_2 + r - 5. \tag{27b}$$

From Eqs. (21), (26a), and (27), the recursion relation for ρ_R is found to be

$$\frac{d\rho_R}{dl} = \rho_R\left(\frac{\epsilon}{2} - 3\rho_R^2\right), \tag{28}$$

where $\epsilon = r - 1$. The form of this equation is equivalent to the coupling constant equation of model A in FNS, though here ϵ is a function of the random driving power index rather than the spatial dimension (cf. Refs. [28], [29]).

Therefore, $r_c = 1$ is the crossover index that divides the system into two universality classes, below which ρ_R has a stable fixed point at 0, and above the stable fixed point is at $\sqrt{\epsilon/6}$. For the case where $r = 1$, it is easy to show that the recursion relation is

$$\frac{d\rho_R}{dl} = -3\rho_R^3. \tag{29}$$

The stable fixed point is thus also at zero though the approaching speed is proportional to $1/\sqrt{l}$. The recursion relation for ν_R can also be determined,

$$\frac{1}{\nu_R}\frac{d\nu_R}{dl} = \begin{cases} c_1 - 4 & \text{if } r \leq 1 \\ c_1 - 4 + \dfrac{\epsilon}{2} & \text{if } r > 1 \end{cases}. \tag{30}$$

With the recursion relations of ν_R, λ_R, D_R, and ρ_R, it is possible to compare the behavior of the diffusion term, nonlinear term, and the random driving in the process of DRG transformation for the two universality classes. With its role analogous to a Reynolds number, ρ_R's attractor at 0 when $\epsilon < 0$ in DRG transformation indicates the increasing dominance of the diffusion term ν_R, while the nonlinear term and the random driving are "absorbed" into the diffusion term. Let λ_R and D_R remain fixed in the DRG transformation, then the scaling exponents c_1 and c_2 can be determined from Eqs. (27),

$$c_1 = 4 - \frac{\epsilon}{2}, \tag{31a}$$

$$c_2 = \frac{\epsilon}{4}. \tag{31b}$$

Then from Eq. (30) it is found that ν_R increases exponentially at the rate $-\epsilon/2$ when $\epsilon < 0$, confirming the increasing dominance of the diffusion term. On the other hand, the random driving becomes critically more dominant in infrared ($k \to 0$) when $\epsilon > 0$, and ρ_R's attractor at $\sqrt{\epsilon/6}$ indicates that the diffusion term becomes comparable with the other terms. This is again confirmed by Eq. (30), with $(1/\nu_R)(d\nu_R/dl) = 0$, when $\epsilon > 0$ using the exponent c_1 in Eq. (30). As mentioned before, the random driving used in LH91 and LHMB corresponds approximately to a spectrum with $r = 0$, and we will thus focus on the universality class $\epsilon < 0$ in the following discussions.

IV. COMPARISONS BETWEEN ANALYSIS AND AVALANCHE MODEL

In this section, quantities predicted by the DRG analysis will be compared with those calculated from the avalanche models. The statistical features of the modified LH91 and LHMB are very similar, and only results from the latter are presented in the discussion.

We first examine the wave number spectrum of the scalar field A. Figure 5 is the power spectrum of A from the avalanche model of LHMB. The spectral slope is -4 at lower wave numbers. This is the value expected for a linear fourth-order hyperdiffusion equation with a random driving and is consistent with the derived avalanche (11) in the continuum limit with a dominant hyperdiffusion term. On the other hand, the power spectrum of the "perturbation" to the linear diffusion field may be conveniently checked by looking at the power spectrum of the transformed field B, because the linear diffusion component of A, a parabola, becomes a dc component of B. From the scaling assumption (23b), $\hat{B}$ may be written as
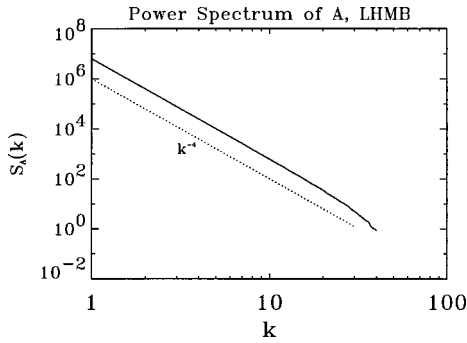
FIG. 5. Wave number power spectrum of A from a representative LHMB model run. The solution is computed for a one-dimensional scalar version of the LHMB avalanche model, defined here on a 100-node lattice. Driving and threshold parameters as in Fig. 2.

$$\hat{B}(k,\omega) = k^{-(c_1+c_2+1)}G_B\left(\frac{\omega}{k^{c_1}}\right),\qquad(32)$$

where G_B is a scaling function. The wave number spectrum of $\hat{B}$ at time t_0 can be obtained by the inverse Fourier transform of Eq. (32) with respect to ω,

$$\hat{B}(k,t_0) = k^{-(c_2+1)}\widetilde{G}_B(t_0 k^{c_1}) = k^{-(3+r)/4}\widetilde{G}_B(t_0 k^{c_1}),\qquad(33)$$

where $\widetilde{G}_B$ is the Fourier integral of G_B, $\int G_B(y)e^{iyt_0 k^{c_1}}dy$. If the system is in statistical equilibrium, $\widetilde{G}_B$ should be approximately independent of the sampling time t_0 and thus also k^{c_1}. The power spectrum of B then has an index of $-3/2$ for $r=0$. Figure 6 shows the power spectrum of B normalized by $k^{-3/2}$ from LHMB. The flatness of the normalized spectrum at larger wave numbers indicates that the agreement is good in that region. The smallest wave number spectrum is subjected to a small wave number cutoff due to the finite size of the spatial domain.

We then calculate the frequency spectra of fall-off energy and total dissipating energy, following HK92. According to Eq. (11), the flux of A is

$$J_A = -\nu\frac{\partial B}{\partial x} - \lambda\frac{\partial B^3}{\partial x}.\qquad(34)$$
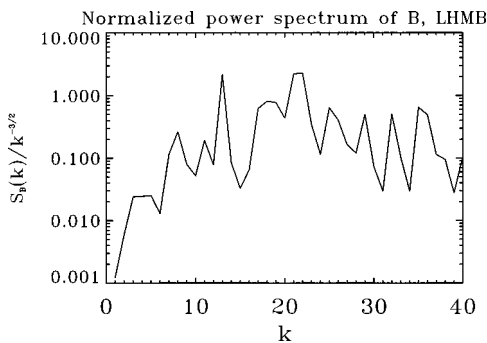

FIG. 6. Wave number power spectrum of B normalized by $k^{-3/2}$, for the same solution as depicted in Fig. 5.

According to the analysis in preceding section, $B\sim x^{\epsilon/4}$ and $\nu\sim x^{-\epsilon/2}$. Then the first term of J_A scales as $x^{-1-\epsilon/4}$ and the second term scales as $x^{-1+3\epsilon/4}$. For $\epsilon<0$, the first term is dominant in the DRG transformation and $J_A\sim x^{c3}\equiv x^{-1-\epsilon/4}$. The fall-off energy can then be written as

$$J_A^2 = x^{2c_3}g_{J_A}\left(\frac{t}{x^{c_1}}\right),\qquad(35)$$

where g_{J_A} is a scaling function. The spectral form of J_A^2 can be found by the Fourier transform (35),

$$\hat{J}_A^2(k,\omega) = k^{-(c_1+2c_3+1)}G_{J_A}\left(\frac{\omega}{k^{c_1}}\right).\qquad(36)$$

The frequency spectrum at x_0 (e.g., boundary point) can then be obtained by the inverse Fourier transform of this equation with respect to k,

$$\hat{J}_A^2(\omega,x_0) = \omega^{-[1+2(c_3/c_1)]}\widetilde{G}_{J_A}(x_0\omega^{1/c_1}),\qquad(37)$$

where $\widetilde{G}_{J_A}$ is the Fourier integral of the scaling function G_{J_A}, $\int y^{-(c_1+2c_3+1)}G_{J_A}(y^{-c_1})e^{iyx_0\omega^{1/c_1}}dy$. If the statistical feature is assumed to be independent of x_0 (e.g., same with those at boundary $x_0=0$), then $\widetilde{G}_{J_A}$ may be considered as a constant and the power-law index is equal to $-2/3$, when $r=0$. This is in good agreement with the fall-off energy spectrum of the avalanche models over the frequency number of 3000 to 20 000, corresponding to time steps of about 100–700, as shown in Fig. 7.

The total energy dissipation can also be calculated by integrating J_A^2 over the whole spatial domain. We employ the same limited area approximation used by HK92:

$$\mathcal{E}(\omega) = \int_0^L dx\int_0^L dx'\int_0^\Lambda dx\,\exp[-ik(x-x')]\hat{J}_a^2(k,\omega)$$
$$\approx \int_0^\Lambda dk\,\frac{k^{-(c_1+2c_3+1)}}{1+(kL)^2}G_{J_A}\left(\frac{\omega}{k^{c_1}}\right),\qquad(38)$$

where L is the size of the domain. Considering the low frequency cutoff due to the finite size of the domain (cf. Fig. 6), we assume that the main contribution of the integration in Eq. (38) comes from higher wave numbers and $(kL)^2\gg1$. In fact, even for wave number 1 $(k=2\pi/L)$, the assumption is already a good approximation because $(kL)^2=(2\pi)^2\gg1$. With this assumption, the integration above gives

$$\mathcal{E}(\omega) = c_\mathcal{E}\omega^{-[1+2(c_3+1/c_1)]},\qquad(39)$$

again the constant $c_\mathcal{E}$ is from the integration of the scaling function. For $r=0$, the power index of the energy dissipation frequency spectrum is $-10/9$. As can be seen from Fig. 8, this index agrees well with that obtained from the avalanche models in the frequency range of frequency number 2000–20 000 (time steps of 100–1000). This frequency range where the continuum limit description is valid and the DRG analysis applies, as shown by these comparisons, corre-
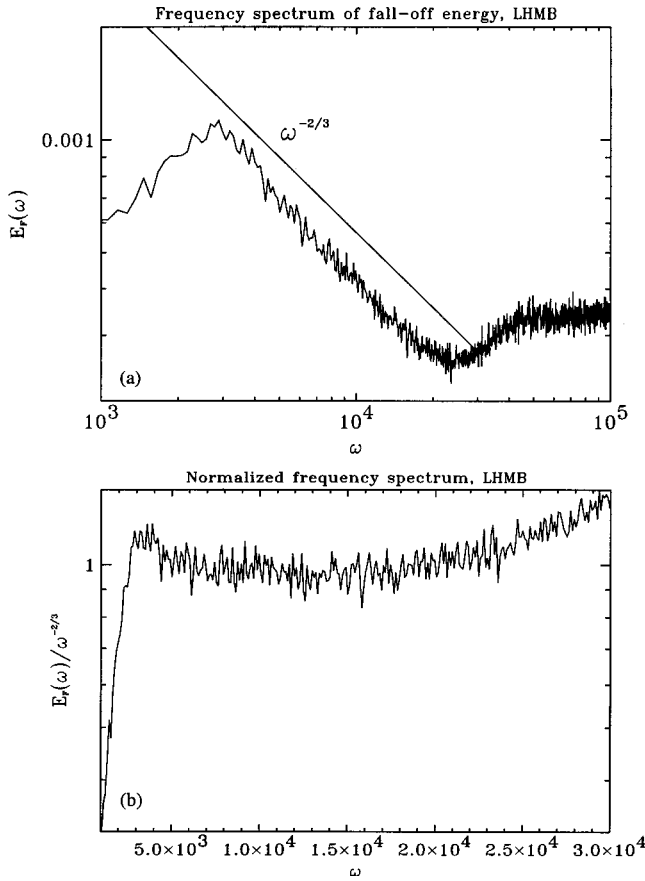
FIG. 7. Frequency spectrum of fall-off energy in the same LHMB solution as in Figs. 5 and 6. Panel (a) shows the raw spectrum, and panel (b) the same spectrum normalized by $\omega^{-2/3}$.

sponds to the interacting avalanche region as categorized by HK92. At higher frequencies (the single-avalanche region) local dynamics becomes dominant and the DRG analysis become invalid, while at lower frequencies (the discharge-event region) the cutoff is associated with the finite size of the domain.

V. DISCUSSION AND CONCLUSION

This study has demonstrated that the curvature-triggered avalanche models proposed in LH91 and LHMB are computationally equivalent to a randomly forced fourth-order hyperdiffusion system subjected to a threshold instability, although LH91 is numerically unstable. The randomly forced fourth-order hyperdiffusive equation is thus the continuum limit of the avalanche models. With the equation in the continuum limit, we are able to achieve a better physical and analytical understanding of the avalanche models. The scale transformation invariants of the equation have been determined through the use of DRG analysis. The scaling exponents of the spectra of certain quantities, including the wave number spectra of scalar fields A and B and frequency spectra of the falling-off energy and dissipating energy, as well as the scaling of the diffusion coefficient and nonlinear coupling coefficients, have been derived from the invariants and are in good agreement with the corresponding quantities ex-
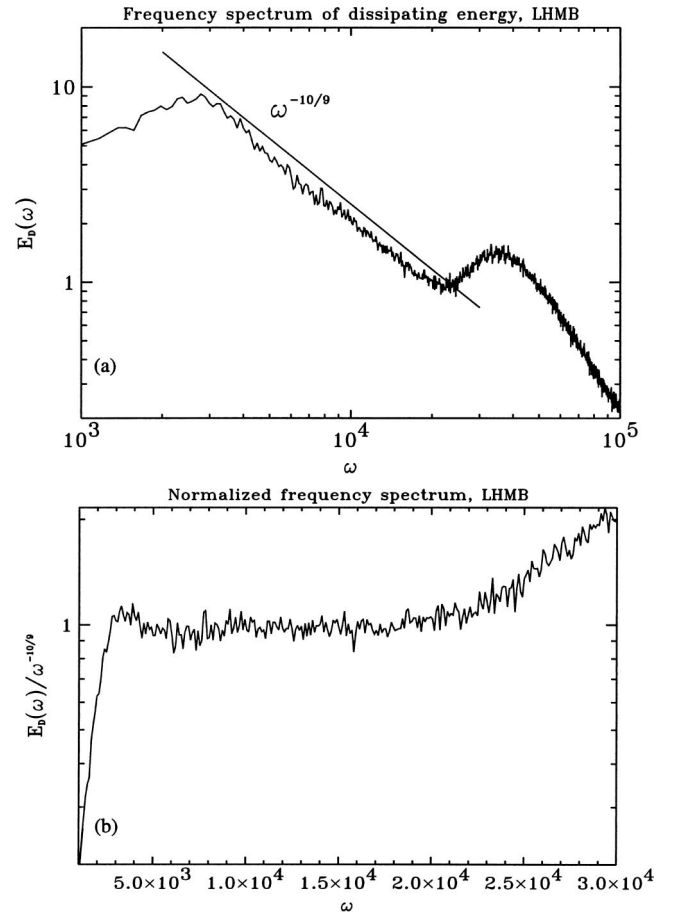

FIG. 8. Frequency spectrum of energy dissipation in the LHMB avalanche model, for the same model run as in Figs. 5–7. Panel (a) shows the raw spectrum, and panel (b) the same spectrum normalized by $\omega^{-10/9}$.

tracted from the avalanche model results in the relevant spectral range. This spectral range where the DRG is valid is constrained by the size of the domain on the small wave number and lower frequency side and the size of the lattice grid on the large wave number and high frequency side. The favorable comparison also provides rigorous support to the interpretation of the avalanche model in the continuum limit.

We conclude this work by briefly discussing some possible links between the avalanche system and the magneto hydrodynamics (MHD) physics believed to be underlying the flaring phenomenon. We start from the induction equation

$$\partial_t \mathbf{B} = \nabla \times (\mathbf{v} \times \mathbf{B}) + \eta \nabla^2 \mathbf{B}, \qquad (40)$$

and assume that we are in a regime strongly dominated by the magnetic field (i.e., strong MHD turbulence) which we take as $\mathbf{B}_0 = (0,0,B)$. In that regime, fluctuations vary mostly in the perpendicular direction, hence we set $\partial_z \equiv 0$. We evaluate the Lorentz force and Ohm's law with these hypotheses, and express further that the velocity field results from an equilibration with the Lorentz force in the momentum equation; integrating over time gives

$$\mathbf{v} \sim \tau \mathbf{j} \times \mathbf{B}, \qquad (41)$$

where τ is a characteristic time of the (slow) evolution of the velocity. Substituting this expression for the velocity field in the induction equation, and furthermore assuming that perpendicular variations are equivalent, i.e., $\partial_x \sim \partial_y \sim \partial$, leads to a model equation that reads

$$\partial_t B \sim B^2 \partial^2 B + \partial B \partial B^2 + \eta \partial^2 B.$$

This is readily rewritten in the form

$$\partial_t B \sim (B^2 + \eta) \partial^2 B + \partial^2 B^3. \tag{42}$$

We now need to compare this with the model (11). Both include a $\partial^2 B^3$ term, but at first glance the first term on the rhs of Eq. (42) is not comparable to the fourth-order term on the rhs of Eq. (11).

In an attempt to resolve this discrepancy, we turn to the theory of strong MHD turbulence (e.g., Ref. [30]). In the solar corona, the magnetic Reynolds number is extremely high, and magnetic reconnection is thus likely to generate turbulence. The linear part of the diffusion term, $\eta \partial^2 B$, can be modified by introducing an eddy diffusivity η_{turb}, the latter computed using two-point closure formulations of strong isotropic (on average) MHD turbulence [30]. It was found there that the only contribution from small-scale fluctuations to dissipation of the large-scale magnetic field stem from the velocity field, averaged on small scales and squared, namely

$$\eta_{\text{turb}} \sim \langle v^2 \rangle. \tag{43}$$

As argued above, in the strong field regime characteristic of the corona, the velocity field results from a balance with the Lorentz force and hence is proportional to the current, i.e., to small-scale gradients [see Eq. (41)]. The predominance of small scales implies

$$\partial_t B \sim \partial^2 B^3 + \eta_{\text{turb}} \partial^2 B. \tag{44}$$

This is somewhat closer to Eq. (11), but by all appearances we are still short by two differentiation orders in the linear diffusive term. However, this term does turn out to be fourth order in a Fourier sense, because in Fourier space, $\eta_{\text{turb}} \sim k^2$ [30]. This implies that the Laplacian in Eq. (44) becomes hyperdiffusive, because of the scale dependence contained in η_{turb}. This thus establishes a suggestive correspon-

dence, at least in Fourier space, between Eq. (11) and the partial differential equations of MHD. Recent study by Diamond and Malkov also suggests hyperdiffusion in the magnetic reconnection [34].

We also note that the Lu-Hamilton interpretation of the avalanche model for MHD in terms of curvature of the field is not to be taken too stringently. The model encompassed in Eqs. (41)–(44) with a turbulent resistivity coefficient involving the current itself in the strong field regime shows how important magnetic field gradients are, irrespective of their being a signature of curvature or not. Indeed, in a standard two-dimensional configuration, corresponding to reconnection events embedded in a strong background field as in the corona and as the lowest-order approximation to reduced MHD, neutral x points develop into x lines and current sheets have a tendency to be straight as shown in numerous numerical simulations [31–33].

If taken at face value, what physical conclusions can be drawn from this correspondence? First and foremost, it implies that the reconnection dynamics is dominated by the magnetic field [viz., Eq. (41)]. Second, once reconnection does occurs, strong MHD turbulence rapidly sets in and dominates transport processes in and out of the reconnection regions. Third, the hyperdiffusive (i.e., fourth-order) character of field dissipation suggests that once reconnection sets in, it is very efficient at dissipating the magnetic field even if the magnetic Reynolds number is very large. Conceptually at least, these conclusions are all compatible with current observational inferences and theoretical understanding of solar flares.

[1] E. N. Parker, Astrophys. J. **264**, 642 (1983).

[2] E. N. Parker, Astrophys. J. **330**, 474 (1988).

[3] E. N. Parker, *Spontaneous Current Sheets in Magnetic Fields* (Oxford University Press, New York, 1994).

[4] E. T. Lu, Astrophys. J. Lett. **446**, L109 (1995).

[5] H. J. Jensen, *Self-Organized Criticality* (Cambridge University Press, Cambridge, 1998).

[6] P. Bak, C. Tang, and K. Wiesenfeld, Phys. Rev. Lett. **59**, 381 (1987).

[7] L. P. Kadanoff, S. R. Nagel, L. Wu, and S. Zhou, Phys. Rev. A **39**, 6524 (1989).

[8] E. T. Lu and R. J. Hamilton, Astrophys. J. Lett. **380**, L89 (1991).

[9] E. T. Lu, R. J. Hamilton, J. M. McTiernan, and K. R. Bromund, Astrophys. J. **412**, 841 (1993).

[10] E. T. Lu, Phys. Rev. Lett. **74**, 2511 (1995).

[11] P. Charbonneau, S. W. McIntosh, H.-L. Liu, and T. J. Bogdan, Sol. Phys. **203**, 321 (2001).

[12] S. D. Edney, P. A. Robinson, and D. Chisholm, Phys. Rev. E **58**, 5395 (1998).

[13] S. W. McIntosh and P. Charbonneau, Astrophys. J. Lett. **563**, L165 (2001).

[14] M. J. Aschwanden and P. Charbonneau, Astrophys. J. Lett. **566**, L59 (2002).

[15] S. W. McIntosh, P. Charbonneau, T. J. Bogdan, H.-L. Liu, and J. P. Norman, Phys. Rev. E **65**, 046125 (2002).

[16] H. Isliker, A. Anastasiadis, D. Vassiliadis, and L. Vlahos, Astron. Astrophys. **335**, 1085 (1998).

[17] D. Vassiliadis, A. Anastasiadis, M. Georgoulis, and L. Vlahos, Astrophys. J. Lett. **509**, L53 (1998).

[18] H. Isliker, A. Anastasiadis, and L. Vlahos, Astron. Astrophys. **363**, 1134 (2000).

[19] H.-C. Chang, Phys. Fluids **29**, 3142 (1986).

[20] S. Boatto, L. P. Kadanoff, and P. Olla, Phys. Rev. E **48**, 4423 (1993).

[21] C. M. Elliott and D. A. French, IMA J. Appl. Math. **38**, 97 (1987).

[22] N. F. Smyth and J. M. Hill, IMA J. Appl. Math. **40**, 73 (1988).

[23] W. H. Press, S. A. Teukolsky, W. T. Vetterling, and B. P. Flannery, *Numerical Recipes* (Cambridge University Press, Cambridge, 1992).

[24] S. K. Ma, *Modern Theory of Critical Phenomena* (Perseus Books, Reading, MA, 1976).

[25] D. Forster, D. R. Nelson, and M. J. Stephen, Phys. Rev. A **16**, 732 (1977).

[26] T. Hwa and M. Kardar, Phys. Rev. A **45**, 7002 (1992).

[27] J. B. Morton and S. Corrsin, J. Stat. Phys. **2**, 153 (1970).

[28] J. D. Fournier, Thése de 3éme cycle, Université de Nice, Nice, France, 1977.

[29] A. Pouquet, J. D. Fournier, and P. L. Sulem, J. Phys. (Paris) **39**, L199 (1978).

[30] A. Pouquet, U. Frisch, and J. Léorat, J. Fluid Mech. **77**, 321 (1976).

[31] D. Biskamp and H. Welter, Phys. Fluids B **1**, 1964 (1989).

[32] H. Politano, A. Pouquet, and P. L. Sulem, Phys. Fluids B **1**, 2330 (1989).

[33] W. H. Matthaeus and S. L. Lamkin, Phys. Fluids **29**, 2513 (1986).

[34] P. H. Diamond, M. Malkov (private communication 2002).